Journal of Physics: Conference Series

PAPER • **OPEN ACCESS**

Investigation of a modified IEA 15MW wind turbine including a winglet with a new mid-fidelity acoustic toolchain

To cite this article: Philipp Seelemeyer and Christina Appel 2024 *J. Phys.: Conf. Ser.* **2767** 022001

Journal of Physics: Conference Series **2767** (2024) 022001 doi:10.1088/1742-6596/2767/2/022001

Investigation of a modified IEA 15MW wind turbine including a winglet with a new mid-fidelity acoustic toolchain

Philipp Seelemeyer and Christina Appel

Deutsches Zentrum für Luft- und Raumfahrt (DLR), Institute of Aerodynamics and Flow Technology, Lilienthalplatz 7, 38108 Braunschweig, Germany

E-mail: philipp.seelemeyer@dlr.de, christina.appel@dlr.de

Abstract. This paper presents the applicability of a new hybrid tool chain for wind turbine rotor turbulent boundary-layer trailing-edge noise (TBL-TEN) to complex rotor geometries. The research introduces a rapid, high-fidelity 2D CFD/CAA method, which enables the assessment of innovative low-noise profile designs concerning TBL-TEN, coupled with a mid-fidelity extrapolation technique for the 3D analysis, aiming to minimize computational time essential for design processes. This procedure is applied here to compare the changes in performance, load distribution and noise reduction if a winglet is added to a large-scale wind turbine, using the example of the IEA Wind TCP Task 47 15-MW-reference turbine [12]. In the first step, a 3D CFD calculation of the entire turbine is performed in order to derive the local flow parameters and thus the input variables for the 2D CAA. These results for the 2D TEN are then extrapolated for the entire turbine using the fast summation and extrapolation method TAP (Turbine acoustic prediction) [1]. As only data for the TEN is included here, only this noise source for the winglet can be analyzed. For a more complete comparison, a 3D scale-resolving simulation was set up for a static wind tunnel situation in order to be able to qualitatively classify the tip/vortex interaction noise that was not recorded by the procedure mentioned above.

1. Introduction

The transformation of the global energy supply towards eco-friendly resources increases the number and size of energy infrastructure. In wind energy, the acceptable locations for new turbines are limited by regulations that take factors like noise emitted by the turbine into account. To open new locations for windfarms and to develop more powerful but quieter wind turbine designs, an aero-acoustic toolchain with suitable fidelity and acceptable runtimes is needed. An extensive approach to a holistic toolchain is presented by Cao et al. [5], which is based on very fast engineering models for flow and sound sources, combined with a high fidelity sound propagation model. The objective of this multi-fidelity toolchain is to examine the positioning of wind turbines in complex surroundings and allows for many computations in the order of minutes. The downside of these fast models lies in limited representation of novel low noise airfoil designs or blade add-ons.

When complex blade designs are to be evaluated, the fidelity of the turbine simulation models has to be increased so that the effect of the add-on can be determined. This requires fast computational fluid dynamics (CFD) for the flow and computational aero acoustics (CAA) for

the noise simulation, both increasing the computational time to multiple hours or days, what makes the design process of new turbine configurations costly. In the German national wind energy project BELARWEA [15, 16] different wingtips, winglets and standard airfoils as well as low-noise airfoils have been investigated experimentally and numerically. Here, 3D CAA methods have been applied and noise source models were extended which led to the development of a 2D mid-fidelity acoustic toolchain, that reduces the computational time to a few hours instead of days. While during the project the work was focused on a non-rotating blade tip at stationary conditions in a wind tunnel environment, the toolchain was extended to applications of full turbines at operating conditions [1].

An overview and limited experimental validation of existent wind turbine noise prediction codes along with detailed code-to-code comparisons with the herein presented approach is part of ongoing work in the IEA Wind TCP Task 39 benchmarking activities, currently limited to TBL-TEN as the dominant noise source and LE/inflow-interaction noise, [2, 3]. Note that modeling approaches to combine non-empirical high-fidelity simulations with fast extrapolation techniques are rare, such are high-quality field validation data which cover all relevant quantities

This paper demonstrates the capabilities of the mid-fidelity acoustic toolchain to estimate the noise benefits from improved blade designs with winglets using the example of a modified IEA 15 MW turbine from Task 47 which has a diameter of 240 m [12]. As a reference for the 2D toolchain, a 3D acoustic simulation is presented and shows the rotation of directivities on the winglet geometry that were previously not captured.

2. Aerodynamic analysis of the modified rotor with added winglet

A 3D CFD Reynolds Averaged Navier-Stokes (RANS) simulation with the well validated and widely used DLR TAU code [19] was performed. The flow conditions follow the first Task47 test cases with an homogeneous inflow speed of 7.5 m/s and nominal rotational speed. The turbine is set up as an isolated rotor without tower or nacelle influence and without any shaft angle to allow for a compressible steady simulation and Menter k-ω-SST turbulence model. The farfield expands 10 diameters up- and downwind. The inner section around the turbine was refined with an unstructured mesh block that encloses the turbine and expands far enough downwind to offer higher resolution for the wake of one full revolution. Each blade is enclosed in a fully structured O-typed cylindrical blade mesh with round cap at the wingtip. To create the blade mesh, an automated script-based approach was used that maintains a consistent mesh quality between simulations of different designs. The non-dimensionalised first layer height y+ is below 1 for the full blade. On each blade, 212 cells in radial direction, 309 cells in profile direction, 13 on the trailing edge and 129 until the edge of the inner chimera boundary (green in Fig. 1) were used. The full simulation contains 50e6 cells and no flexibility of the rotor was regarded.

2.1. Winglet design

When considering existing winglet optimizations, the objective on increased performance leads to winglet spans of up to 10% with respect to the rotor radius [8] [13]. However, modern industrial designs of common wind turbines like the Enercon E-82 or E-115 are fitted with significantly smaller winglets, shorter than one chord length of the tip section, resulting in spans of around 1-2%R. This originates from taking loads along the blade into consideration, for which bigger winglet sizes would exceed structural limits [21]. Therefore for this study the geometrical outlines found by Johansen [18] were used. The winglet span was fixed to 1.2 m (1%R). The forward sweep of the winglet is set to keep the line of the maximum profile thickness perpendicular to the wing. The winglet cant angle is 84 deg pointing upwind to allow for more tower clearance. The twist distribution changes linear from base to top. Three different designs with twist angles from -4 deg (reduced angle of attack (AoA)), 0 deg and +4 deg (increased AoA) were investigated. As seen in Fig. 2, the winglet does not change the projected radius of the blade but increases the

wetted area. As profile the FFA-W3-211 from the IEA 15MW turbine definition was maintained. The parametric blade tip was modelled including a closed and curvature consistent tip section as well as finite trailing edge thickness.

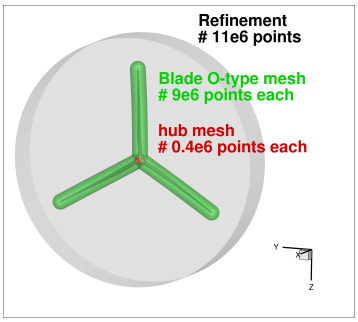

Figure 1: Components of 3D CFD simulation, background mesh not shown

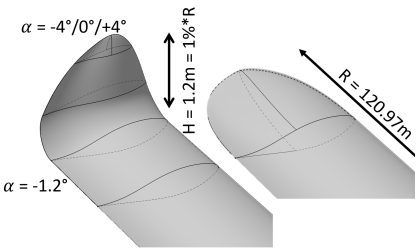

Figure 2: Winglet and reference wing

2.2. Performance investigation

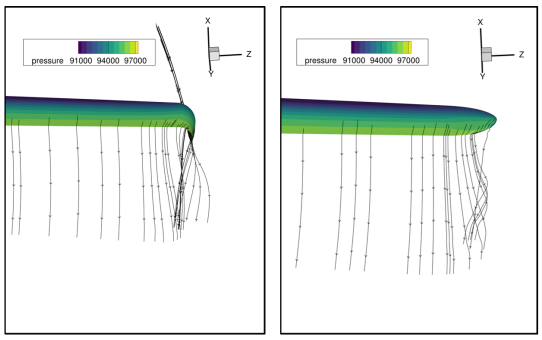

Figure 3: Streamtraces showing tip vortex, -4° twist winglet vs. reference wing

Besides the objective of increasing the torque for higher energy output, pressure forces and moments on the rotor and especially around the outer blade sections have to be regarded. Fig. 5 shows the load distribution in thrust force Fx, torque Mx and the resulting power output per radius. The winglet influences the flow on the blade to round 90% r/R inboard from the blade tip. Besides higher torque output, the thrust force in the outer blade sections is also increased what leads to overall higher structural loads. The effect on global performance for all three winglet designs is shown in Table 1. While just the winglet with -4 deg twist shows slightly lower performance increase, both the 0 deg and +4 deg twisted designs show the exact same torque and thrust force. One can observe the beneficial effect that alongside the increase in torque the thrust force only increases by half the amount of torque, what relatively can relieve the structure of the blade. The comparison furthermore shows that the beneficial effect of the winglet results mainly from the improved flow conditions for the blade in the outer radial area by reducing three-dimensional flow components. Due to the large cant angle of the winglet, resulting local forces on the winglet itself point into the radial direction of the blade and thus do not contribute to torque or thrust force. The flow around the winglet is shown in Fig. 3 with streamtraces and in Fig. 4 with pressure distributions at sections with equal chord length and is further investigated for the aeroacoustic simulation.

3. Aeroacoustic analysis

The overall noise emission of wind turbine blades can be divided into five relevant noise sources, two of which are turbulent boundary-layer trailing-edge noise (TBL-TEN) and tip vortex noise. For each source, individual noise reduction techniques have been developed [7]. To reduce overall noise emissions, some objectives of winglet design are to decrease the tip vortex intensity, reduce the interaction between the tip vortex and the blade geometry as well as to reduce turbulent

Table 1: Moment Mx and downwind thrust force Fx for reference and winglet at 7.5 m/s wind

	Mx $[Nm]$	Fx $[N]$
Reference	9.933 e6	1.184 e6
Winglet twist -4 *deg*	9.990 e6 (+0.57%)	1.188 e6 (+0.34%)
Winglet twist 0 *deg*	9.995 e6 (+0.62%)	1.188 e6 (+0.34%)
Winglet twist $+4$ *deg*	9.995 e6 (+0.62%)	1.188 e6 (+0.34%)

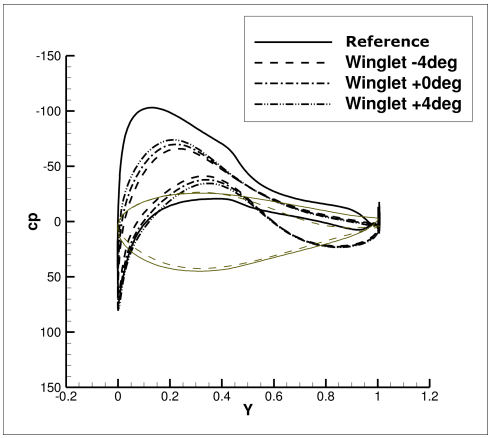

Figure 4: Pressure distribution on stations with equal chord length

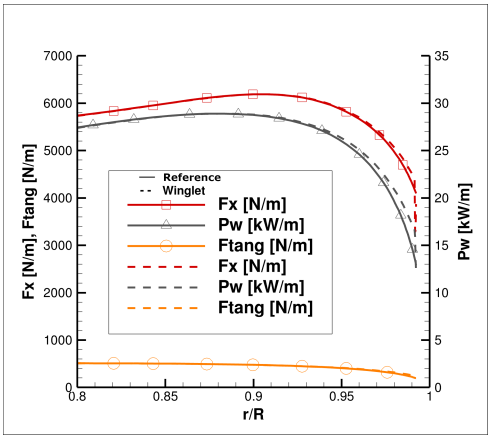

Figure 5: Radial loads, outboard wing, winglet twist -4deg

flow components to weaken TBL-TEN. Nevertheless, adding a winglet to the blade increases the overall TE length and increases the area where TBL-TEN is emitted. Furthermore, the winglet related directivities are rotated by 90° and radiate, while the blade is at the lowest position, in ground direction. While the reference blade geometry shows highly three-dimensional flow around the tip followed by a clearly visible eddy rolling inwards, the flow behind the winglet is steadier. Along the flat outer blade section, the flow remains mostly two dimensional and the eddy shows less intensity. Despite all three winglet twist distributions showing mostly the same global performance, the pressure distribution on the winglet changes with modified twist angle. Since the deflection of the tip vortex away from the rotor center is expected to show the best aeroacoustic noise reduction and only slight penalties in performance, the winglet with -4° twist will be further investigated.

The high-fidelity part is a hybrid CFD/CAA (computational fluid dynamics/computational aeroacoustics) toolchain, which models the acoustic sources based on a CFD simulation and propagates the sound via a CAA computation. The CAA simulations are based on the APE-4 (acoustic perturbation equation) system with dominating vortex sound source. Acoustical source generation is achieved using the FRPM [11] (fast random particle mesh) method. For the solution of the perturbation equation system the DLR CAA code PIANO [6] is applied. Spatial discretization is based on the DRP (dispersion-relation-preserving) scheme of Tam & Webb [20] and the explicit time integration is done with an alternating LDDRK scheme [17]. For the acoustic vortex source the fluctuating linearized Lamb vector L_i' is modeled: $L_i' = -\epsilon_{ijk}\omega_j^0 v_k^t - \epsilon_{ijk}\omega_j^t v_k^0$. Here the index 0 denotes the magnitudes of the base flow, the index t those of the turbulence statistics and the prime indicates fluctuating quantities, v is the velocity and ω is the turbulent dissipation rate. ϵ_{ijk} is the Levi-Civita symbol. An intensive numerical and experimental study including validation data of this method has been published in [10].

To minimize the numerical effort without switching to semi-empirical methods, the 3D blade is broken down into single 2D slices. The necessary 2D computations can be fulfilled e.g. on a single 64 CPU HPC node in less than 20h. To translate the 3D flow behavior from the CFD rotor simulation into 2D slices, the local aerodynamic AoA on each slice is determined by using the annulus ring method presented by Hansen [14]. Once the 2D CFD/CAA computations are done, the simulated TBL-TEN directivities can be used to be superposed and rotated to finally get a spectral result, an OASPL (overall sound pressure level) or a noise signature for the complete turbine. Therefore, additional turbine parameters like tower height, precone, tilt, rotational velocity and wind speed are considered. In the next step the beam angles of each trailing edge position related to the defined observed are calculated over rotor revolution. With this information the correct contributions of the directivities, provided by the 2D CAA computations, can be read out and superposed for all rotor blade segments. It was shown, that a number of 10-12 slices in the outer third of the blade is sufficient to get a meaningful prediction for a wind turbine. In detail this procedure is described in [1]. A detailed comparison with other codes and experimental validation data is shown in the publication by Bertagnolio et al. [2].

3.1. Estimation of sound propagation and superposition

As the influence of the winglet on the blade flow can be determined from the 3D CFD, four slices have been chosen to cover the part of the blade, where flow differences between configurations w/o winglet can be observed. The objective is to show the influence of the winglet on TBL-TEN contribution. The slices are depicted in Fig.6. The slices $c1$-$c4$ refer to the reference or reference blade. $c1w$-$c4w$ and $c13$-$c16$ belong to the configuration with winglet. The slices $c5$-$c10$ and the related flow conditions are equal for both configurations and are important to cover the whole turbine. The aerodynamic effect of the winglet on the aerodynamic incident angle compared to the reference configuration is shown in Fig 7. The flow on the outboard section of the blade shows a reduction of up to 0.2° in AoA, what leads to lower pressure differences and thus lower aeroacoustic noise emission. The reduction in AoA is related to a reduced flow velocity around the winglet that lowers from approx. 67.55 m/s to 67.53 m/s.

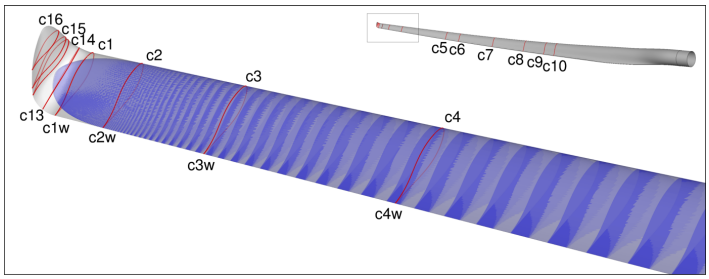

Figure 6: Reference (blue) and winglet (grey) blade geometry with considered 2D CAA slices (red lines)

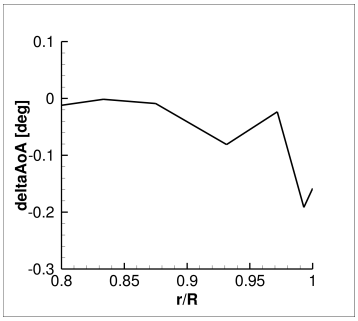

Figure 7: Difference in incident angle, winglet, from 3D CFD

As an intermediary result the 1/3-octave band spectrum of the considered slices are shown in Fig. 8 and 9. Note, that these spectra include the local flow conditions at the radial blade position at the given operational point only, but not the influence of the segment width or the radiation angle. All spectra are normalized to a reference width of 1m, a distance of 1m and 90° below the trailing edge and perpendicular to the inflow direction.

As the winglet slightly increases the loads at the outboard section (Fig. 5), a shift of the sound pressure level (SPL) spectra towards lower frequencies from 235 Hz to 140 Hz can be observed for the most outboard slice c1 / c1w. This effect is increased by the overall larger chord length

of the profiles in the winglet case. A direct decrease of the SPL cannot be observed, but in combination with an acoustic A-rating the differences are emphasized and can be relevant for certification. As the slices c2 to c4 are further inboard, the effect of the winglet flow on the further inboard sections is reduced and the effect on the spectra is also reduced. Following from that the slices $c5$ to $c10$ can be treated as common slices for both configuration and a separate CAA computation is not necessary.

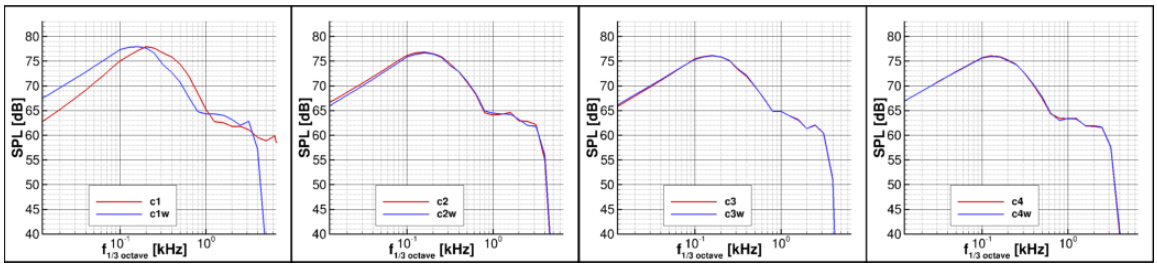

Figure 8: TBL-TEN spectra, 90° below TE, normalized to a distance of 1m and a span width of 1m

Looking at the related 1/3-octave band spectra for the winglet exclusively (Fig. 9) it is remarkable that slice $c13$ shows different spectral characteristics than $c14$ to $c16$. But the flow conditions change rapidly for these two slice groups as $c13$ is located at the bow of the winglet with an effective AoA of about 8° with a strong loading of the boundary layer compared to $c14$ to $c16$ with only 2.5°.

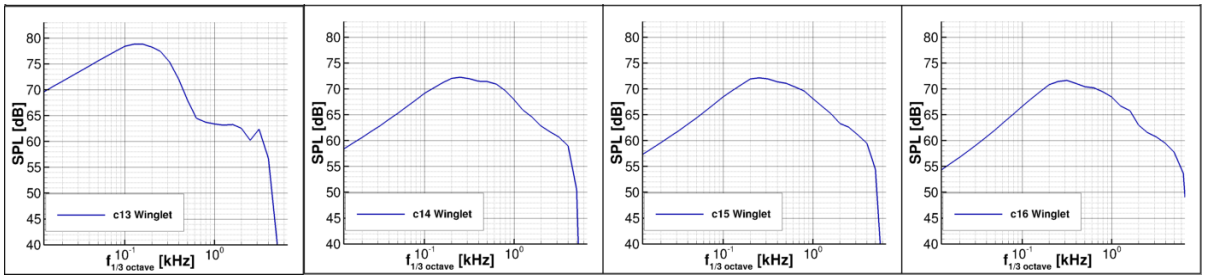

Figure 9: TBL-TEN spectra only for the slices directly at the winglet $c13$-$c16$, 90° below TE, normalized to a distance of 1m and a span width of 1m

3.2. Winglet effects on noise propagation

To estimate the winglet's impact with an explicit value, the 2D 1/3-octave band spectra were extrapolated and summarized at the IEC certification position. This position is located directly downwind on the ground at a distance equal to the tower height (here 150m). The related third octave spectra are shown in Fig. 10 and 11. Although the winglet configuration has a longer trailing edge and therefore more contribution to noise, the smoother flow conditions can compensate the additional TBL-TEN source length. The benefit in the SPL maxima is 1 dB for the winglet configuration. By applying an A weighting (Fig. 11) the difference between both configurations is emphasized. Note that the flow conditions and related CAA results of the remaining slices $c5$ to $c10$ have been kept the same for both configurations, since a meaningful influence of the winglet can only be observed at the outer four slices.

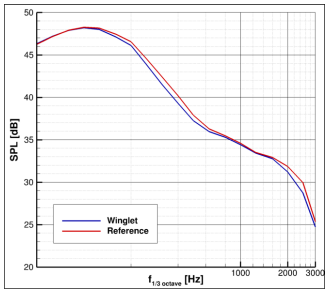

Figure 10: 1/3-octave-band spectrum, certification position 150m downwind of turbine, ground-level, averaged over one revolution

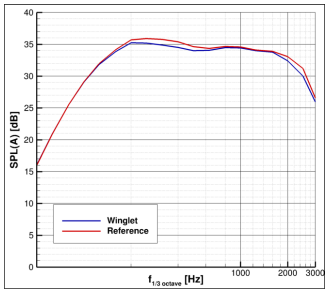

Figure 11: A-rated 1/3-octave-band spectrum, certification position with same conditions as in Fig. 10

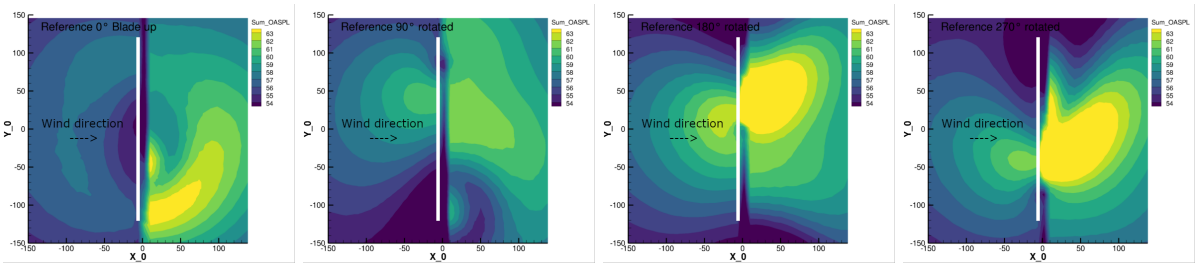

Figure 12: OASPL noise maps for the reference configuration. Turbine is located at (0/0), blade positions 0° (up), 90°, 180° (down), 270°.

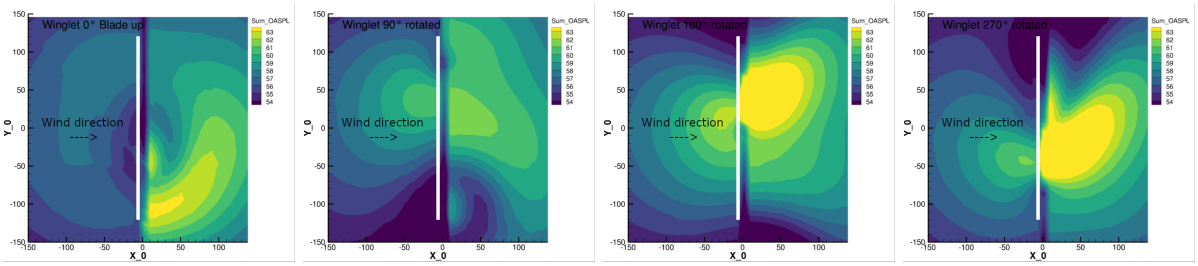

Figure 13: OASPL noise maps for the winglet configuration. Turbine is located at (0/0), blade positions 0° (up), 90°, 180° (down), 270°.

Another approach to analyze both configurations is by plotting a noise signature map for e.g. the overall sound pressure level (OASPL). In Fig. 12 and 13, the OASPL is resolved over the rotor revolution with positions up (0°) and additional at 90°, down 180°, and 270°. It is observed that there is a decrease in OASPL for all blade positions, with the largest reduction in the up- and 90° azimuts.

By averaging the sound pressure level over one full rotor revolution, the mean OASPL is shown in Fig. 14 and 15. The noise reduction of peak OASPL at the suction side (downwind) of the turbine becomes clearly visible in the difference plot Fig. 16 where the averaged OASPL values for winglet and reference configuration are subtracted. However the upwind side, where the OASPL is considerably lower, remains nearly unaffected.

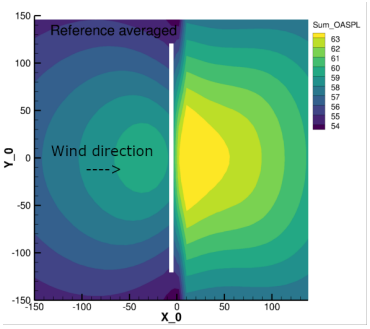

Figure 14: Averaged OASPL noise map for the reference configuration.

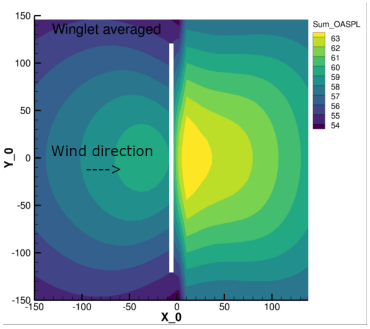

Figure 15: Averaged OASPL noise map for the winglet configuration.

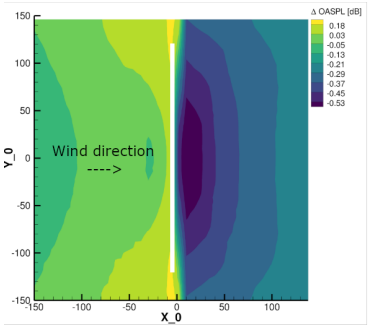

Figure 16: Difference of the averaged OASPL noise maps for both configurations.

To put acoustic effects beyond TBL-TEN from the 2D toolchain into perspective, the commercial aero-acoustic solver MGLET [4] was used. It features a hybrid approach, in which acoustic splitting methods solve the incompressible Navier-Stokes equations together with acoustic perturbation equations [9] and is able to determine geometrical influences. Due to the numerical effort, only the tip section of the blade was calculated. For both cases the flow conditions have been set to constant values: AoA = 4°and flow velocity = 67 m/s, meaning that the influence of the winglet on global flow conditions (as in Fig. 7) is neglected. This is an important issue, since a main winglet effect on the acoustic is based on the improved flow conditions at the outboard section. The mesh sizes were 240e6 cells for the winglet and 170e6 cells for the reference geometry. The computation time was each 7h on 2176 CPUs for the winglet and 1536 CPUs for the reference. The current method has been substantially validated for the TBL-TEN source contributions and to a limited extent for other existing sources, applying wind tunnel and field test data. New field test facilities like the WiValdi research wind farm in north Germany are expected to expand current validation possibilities for complex rotor geometries.

Since the largest effect on TBL-TEN emission from the 2D toolchain was seen for frequencies around 100 and 200 Hz (Fig. 10), corresponding contour plots of the acoustic pressure in different planes will be compared in 3D simulations with MGLET.

The power spectral densities (PSD) in dB for the 100Hz, 200HHz, 300Hz and 1000Hz third-octave bands in x=0 plane are depicted in Fig. 17 (reference blade) and Fig. 18 (blade with winglet). The increased PSD directly at the blade root position is a result of the applied sponge layer surrounding the whole computational domain. Both configurations show overall similar emission characteristics while the winglet increases PSD levels especially in areas with high pressure gradient, e.g. on suction and pressure side of the wing as well as the inner radius of the winglet. Due to the orientation of the airfoil, e.g. 90° rotated at the winglet, the directivities change. Furthermore, the contribution of the very low frequency PSD is reduced at the winglet tip, since the chord length is rather short. In contrast to this the 1kHz PSD plots show an increase for the winglet. But note, that color legend is changed for these 1kHz plots. The absolute contribution of this 1/3-octave band is significantly smaller. In addition to the PSD plots, virtual microphones were placed within the 3D domain. These were analyzed analogously to the 2D CAA simulations in Fig. 8 with the objective to compare the tip vortex interaction noise between reference and winglet. However, the simulated real time was not sampled long enough to produce reliable spectra. Therefore the spectra were not shown here. Nonetheless, the noise reduction of the wing with winglet compared to the reference configuration from the 2D CAA computations could be confirmed qualitatively and with regard to the delta SPL.

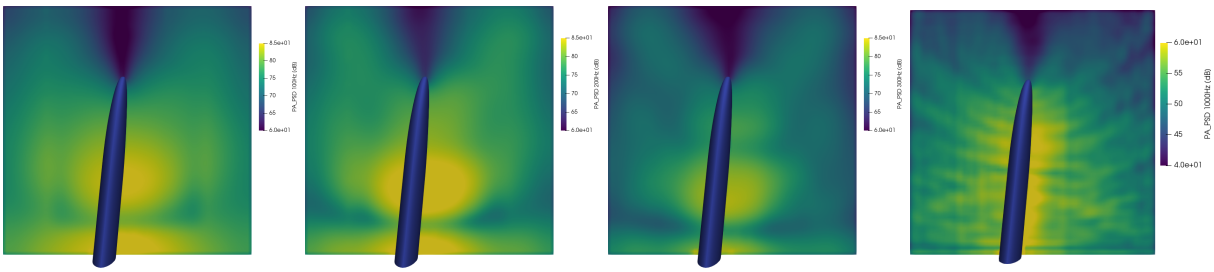

Figure 17: PSD of acoustic pressure in dB of 100, 200, 300, 1000Hz third-octave band (from left to right) for reference configuration, at x=0 plane.

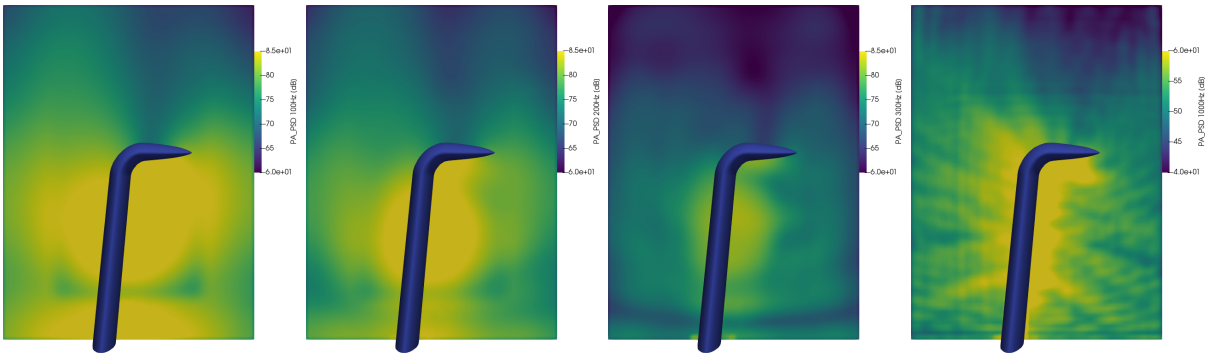

Figure 18: PSD of acoustic pressure in dB of 100, 200, 300, 1000Hz third-octave band (from left to right) for winglet configuration, at x=0 plane.

4. Conclusion and Outlook

Adding a winglet to the IEA 15 MW wind turbine showed an increase in torque and only minor additional thrust on the rotor. Although the present geometry achieved a promising increase in performance, a full winglet shape optimization with respect to aeroacoustics might result in a better performing blade design. However, compared to the performance increase obtained in the publication that delivered the winglet shape [18], the increase in power output for this turbine remains below the expectations. This likely results from the small scale of the winglet compared to the very large-scale of the turbine.

The 2D acoustic simulation was limited on TBL-TEN sources and did not consider vortex-wake or vortex-blade interactions. The simplified 2D CFD calculations in the acoustic toolchain were carried out without investigating the effect of the winglet on the transition point at the blade or the effect of the winglet on stabilizing the boundary layer to prevent separation. Both configurations were calculated with fully turbulent flow to ensure better comparability. The 3D calculation neglects the rotation of the blades and also the altered flow conditions as a result of the winglet, which beforehand prove to be of a relevant size. The effect of additional TBL-TEN sources by the winglet itself is reproduced well qualitatively. Although the 2D extrapolation toolchain may not directly consider shielding effects of the geometry, it accounts for the impact of the winglet's rotated directional characteristics.

With regard to the 3D pressure distributions in Fig. 7, a TBL-TEN reduction can be assumed, as the winglet significantly reduces the suction peaks and thus also the load in this section. Since the extraction method according to Hansen [14] only showed a difference of approx. 0.2° in the effective AoA, the TBL-TEN level in this 2D section should be reduced even more than calculated by the 2D CAA with respect to the pressure distributions. With the BEM methods available for the present study, a blade with a winglet could not be processed and an iterative

recalculation with the aim of reproducing the 3D pressure distribution in 2D was deliberately omitted for reasons of time. However, for future work a review of the used method and extension to matching 3D pressure distributions in the 2D case is recommended. Despite these limitations and the prediction of minor noise reduction, the winglet improves the flow quality as it reduces the overall AoA and smoothes streamlines and pressure distributions, what globally results in a total reduction in noise emissions. The simplified CFD/CAA toolchain is capable of detecting the positive influence of the winglet on the dominant aeroacoustic noise source and allows for fast and simple comparisons between different designs with small computational resources.

5. Acknowledgments

The authors thank Johannes Kreuzinger and his team from Kreuzinger + Manhart Turbulenz GmbH for providing the flow and aeroacoustic solver MGLET.

References

[1] Appel C 2023 *Noise prediction for wind energy turbines based on CAA methods* (Dublin: Wind Turbine Noise)
[2] Bertagnolio F and Fischer A et al 2023 *Wind turbine noise code benchmark: A comparison and verification exercise* (Dublin: Wind Turbine Noise)
[3] Casalino D and van der Velden W et al 2022 *A Framework for Multi-Fidelity Wind-Turbine Aeroacoustic Simulations* (Southampton: AIAA 2022-2892)
[4] Bharadwaj A V and Dierke J et al 2022 *Wall-Modelled LES on Hierarchical Cartesian Mesh for Trailing Edge Noise Prediction* (Southampton: AIAA 2022-2801)
[5] Cao J and Nyborg C M et al 2022 *A new multi-fidelity flow-acoustics simulation framework for wind farm application* (Renewable and Sustainable Energy Reviews 156)
[6] Delfs, J. W. et al 2008 *Numerical simulation of aerodynamic noise with DLR's aeroacoustic code PIANO* (Manual of PIANO version 5.2; DLR Braunschweig)
[7] Deshmukh S and Bhattacharya S et al 2018 *Wind turbine noise and its mitigation techniques: A review* (Sydney: 2nd International Conference on Energy and Power)
[8] Ebrahimi A and Mardani R 2018 *Tip-vortex noise reduction of a wind turbine using a winglet* (Journal of Energy Engineering)
[9] Ewert R and Kreuzinger J 2021 *Hydrodynamic/acoustic splitting approach with flow-acoustic feedback for universal subsonic noise computation* (Journal of Computational Physics)
[10] Ewert R and Appel C et al 2009 *RANS/CAA Based Prediction of NACA 0012 Broadband Trailing Edge Noise and Experimental Validation* (Miami: AIAA 2009-3269)
[11] Ewert R 2007 *RPM - the fast Random Particle-Mesh method to realize unsteady turbulent sound sources and velocity fields for CAA applications* (Rome: AIAA 2007-3506)
[12] Gaertner E and Rinker J et al 2020 *IEA wind TCP task 47: definition of the IEA 15-megawatt offshore reference wind turbine* (National Renewable Energy Lab. (NREL))
[13] Hansen T H and Muehle F 2018 *Winglet optimization for a model-scale wind turbine* (Wind Energy)
[14] Hansen M and Sørensen N et al 1998 *Extraction of lift, drag and angle of attack from computed 3-D viscous flow around a rotating blade* (Dublin: European Wind Energy Conference)
[15] Herr M and Rohardt C H et al 2019 *Aeroacoustic Assessment of Wind Turbine Blade Tips* (Lisbon: 8th International Conference on Wind Turbine Noise)
[16] Herr M and Ewert R et al 2016 *Low-Noise Technologies for Wind Turbine Blades* (Danzig: Wind Turbine Sound)
[17] Hu F Q and Hussaini M Y 1996 *Low-dissipation and low-dispersion Runge–Kutta schemes for computational acoustics* (J Comp Phys 124, 177–191)
[18] Johansen J and Sørensen N 2007 *Numerical analysis of winglets on wind turbine blades using CFD* (European Wind Energy Congress)
[19] Schwamborn D and Gerhold T 2006 *The DLR TAU-code: recent applications in research and industry* (Delft: ECCOMAS CDF)
[20] Tam C and Webb J 1993 *Dispersion-relation-preserving finite difference schemes for computational acoustics* (J Comp Phys 107, 262–281)
[21] Zahle F and Sørensen N et al 2018 *Computational fluid dynamics-based surrogate optimization of a wind turbine blade tip extension for maximising energy production* (IOP Conf. Series: Journal of Physics)